Journal of Renewable
Materials

Tech Science Press

Doi:10.32604/jrm.2025.02025-0096

ARTICLE

Bio-Derived Tannin-Modified Phenolic Carbon Cryogels with Optimized Microstructure for Supercapacitors Application

Zhiying Lin[1], **Boju Deng**[1], **Qianqian Zhang**[1], **Jingming Chen**[2], **Xinqiang Ye**[3], **Yuling Lan**[1], **Jiuping Rao**[1,*], **Mizi Fan**[4] and **Weigang Zhao**[1,*]

[1]College of Material Engineering, Fujian Agriculture and Forestry University, 63 Xiyuangong Road, Fuzhou, 350002, China
[2]Fujian Super Tech Advanced Material Co., Ltd., No. 5 Industrial Second Road, Liancheng Industrial Zone, Longyan, 366299, China
[3]Fujian Yongan Forestry (Group) Co., Ltd., No. 819 Yanjiang East Road, Yong'an, 366000, China
[4]College of Engineering, Design and Physical Sciences, Brunel University, Uxbridge, London, UB8 3PH, UK

*Corresponding Authors: Jiuping Rao. Email: rjustin@fafu.edu.cn; Weigang Zhao. Email: weigang-zhao@fafu.edu.cn

Received: 30 April 2025; Accepted: 01 July 2025; Published: 28 May 2026

ABSTRACT: Bio-derived carbon cryogels have garnered significant interest as promising electrode materials for supercapacitors due to their high specific surface area (SSA), hierarchical porosity, and eco-friendly synthesis methods. In this study, a tannin-modified phenolic hydrogel was synthesized using a sustainable tannin–phenol precursor system and subsequently subjected to three distinct drying methods-freeze-drying (FD), supercritical drying (SCD), and ambient pressure drying (APD)-to systematically evaluate their influence on structural integrity, porosity, and electrochemical behavior. Among these, the sample obtained via freeze-drying (TPUF-FD) maintained the most intact porous network, minimizing structural collapse during sublimation of ice under vacuum. This preservation of hierarchical micro- and mesopores facilitated enhanced ion diffusion, leading to the highest SSA and favorable nitrogen/oxygen functionalities that contribute to both electric double-layer capacitance and pseudocapacitance. The TPUF-FD electrode exhibited a high specific capacitance of 127.6 F g^{-1} at 0.5 A g^{-1}, maintaining 107.0 F g^{-1} at 10 A g^{-1}, which corresponds to a rate retention of 83.9%. When assembled into a symmetric device, the supercapacitor achieved an energy density of 8.47 Wh kg^{-1} at a power density of 562.5 W kg^{-1}. Notably, the device retained 100% of its initial capacitance after 9000 charge–discharge cycles at 10 A g^{-1} with excellent coulombic efficiency (108.3%). These results underscore the crucial role of freeze-drying in preserving both the microstructural features and surface chemistry of biomass-derived carbon cryogels, which enhances ion accessibility and contributes to the stable, high-performance supercapacitor applications.

KEYWORDS: Tannin-derived carbon cryogels; freeze-drying; porous structure engineering; biomass-based electrode materials; supercapacitors; electrochemical performance

1 Introduction

The excessive reliance on fossil fuels has led to severe environmental degradation and the rapid depletion of non-renewable resources. To address the escalating energy and environmental crises, global attention is shifting toward sustainable energy technologies and green energy storage systems [1]. Renewable energy sources-such as solar, wind, and hydroelectric-offer promising alternatives; however, their intermittent and unstable nature demands the development of efficient, durable, and eco-friendly energy storage devices [2].

Supercapacitors have emerged as a leading class of electrochemical energy storage devices due to their high power density, rapid charge/discharge rates, long cycling stability, and minimal environmental footprint [3]. Based on their energy storage mechanisms and electrode material types, supercapacitors are generally categorized into electric double-layer capacitors (EDLCs) [4], pseudocapacitors (PCs) [5], and hybrid supercapacitors (HSCs) [6,7]. EDLCs store energy via the electrostatic accumulation of ions at the electrode–electrolyte interface, which is strongly influenced by the specific surface area and porosity of the electrode material [8]. Widely used materials for EDLCs include activated carbon, carbon nanotubes, and aerogels. For instance, Sruthy et al. [9] prepared graphitic activated carbon from pine wood residue using boron-assisted graphitization and a two-step carbonization method with KOH activation at 900°C, demonstrating excellent capacitive performance. Pseudocapacitors, in contrast, rely on fast faradaic redox reactions but often suffer from limited cycling life due to structural degradation [10]. Hybrid capacitors aim to integrate the strengths of both types but are constrained by electrode mismatching and the use of flammable organic electrolytes, which pose safety and scalability challenges [11]. Therefore, the rational design of electrode materials with high conductivity, tunable porosity, and low environmental impact is essential—among which carbon cryogels have shown considerable promise.

Carbon cryogels [12,13], as promising EDLC materials, combine ultralight weight, high electrical conductivity, chemical stability, and a tunable hierarchical pore network. These materials typically possess specific surface areas ranging from 350 to 900 m^2 g^{-1}, enabling fast charge transport and high ion-accessible surface area [14]. Carbon aerogels are generally synthesized through a sol-gel condensation reaction involving monomers (e.g., resorcinol or phenol) and crosslinkers (e.g., formaldehyde) to form three-dimensional polymer networks [15,16]. The phenolic hydroxyl groups (-OH) in phenol enable it to undergo polycondensation reactions with formaldehyde, producing phenolic resins with robust structural frameworks. Several studies have explored biomass-based aerogels for energy applications. For example, Wang et al. [17] prepared lignin-derived carbon aerogels via sol-gel synthesis and reported well-developed porosity and excellent electrochemical properties.

Tannin, a naturally abundant polyphenol from plant sources such as bark and fruit, exhibits a similar chemical structure and reactivity, making it an effective and greener substitute for phenol [18]. Notably, tannin is significantly more economical (≈14 ¥ kg^{-1}) compared to phenol (≈108.62 ¥ kg^{-1}), enhancing the cost-effectiveness of the final material. Thus, tannin-based phenolic resins not only lower synthesis costs but also align with green chemistry principles and support the development of environmentally sustainable materials with high market potential [19]. By partially substituting phenol/resorcinol with condensed tannins, the resulting carbon cryogels retain high surface area (up to 788.42 m^2 g^{-1}) while significantly reducing environmental toxicity. Thus, tannin-based phenolic resins not only lower synthesis costs but also reduce environmental toxicity, aligning well with the principles of green chemistry [20,21]. Braghiroli et al. [22] further demonstrated that tannin-derived nitrogen-doped aerogels prepared via hydrothermal treatment delivered excellent specific capacitance. However, a systematic comparison of drying methods on the pore architecture and performance of tannin-based carbon aerogels remains lacking in the literature.

A critical step in the preparation of carbon cryogels is the drying of the wet gel, which largely determines the integrity of the porous network. Improper drying can induce structural collapse due to capillary forces generated during solvent evaporation. Three main drying techniques are commonly used: ambient pressure drying (APD), supercritical drying (SCD), and freeze-drying (FD) [23]. Aerogels synthesized by different drying methods vary, such as supercritical drying (aerogels), freeze-drying (cryogels), and atmospheric pressure drying (xerogels). APD often results in significant shrinkage and pore collapse due to high surface tension. In contrast, SCD eliminates surface tension by raising the solvent above its critical point. Since the solvent has no surface tension in the supercritical state, no capillary pressure is generated, thus avoiding the collapse of the gel structure. FD removes the solvent through the sublimation of the freezing solvent, thereby avoiding the liquid-gas interface that causes capillary stress. During the freeze-drying process, the moisture in the solution gradually forms ice crystals. These ice crystals leave pores during the sublimation process, thus forming a porous structure. The size and shape of the pores depend on the freezing rate and temperature. A faster freezing rate usually leads to the formation of smaller ice crystals, thereby achieving a more uniform pore structure. Among these, freeze-drying is particularly attractive for biomass-derived systems due to its mild conditions, energy efficiency, and ability to preserve delicate pore architectures without chemical additives. After drying, the organic cryogels undergo carbonization in an inert atmosphere to convert the polymeric network into a conductive carbon framework [24]. Additionally, the dilution ratio of the resin to solvent is a key parameter that affects the polymer network formation, pore morphology, and final electrochemical properties.

In light of the growing demand for sustainable and high-performance electrode materials, this work introduces a green and renewable precursor system by partially substituting phenol with bio-derived tannin to synthesize tannin-modified phenolic hydrogels. To the best of our knowledge, few studies have systematically compared the effects of different drying techniques on the structural integrity and electrochemical performance of biomass-derived carbon aerogels. Herein, three distinct drying methods—freeze-drying (FD), supercritical drying (SCD), and ambient pressure drying (APD)—are employed to tailor the microstructure and pore characteristics of the resulting carbon aerogels. This study uniquely demonstrates that freeze-drying can effectively preserve the fragile gel network, yielding hierarchical porosity with a high specific surface area and excellent ion transport properties. Moreover, the optimized carbon aerogel exhibits superior specific capacitance and cycling stability in both three-electrode and two-electrode systems. These findings offer new insights into the structure–performance relationship of bio-based carbon aerogels and highlight their promising potential as next-generation supercapacitor electrodes.

2 Experimental

2.1 Reagents and Materials

Condensed tannin (from quebracho wood, 70 ± 2.0% purity, 4%–5% moisture content) was supplied by Xinhua Co., Ltd. (China). Formaldehyde solution (CH_2O, 37.0 wt.%), phenol (C_6H_5OH), urea ($CO(NH_2)_2$), sodium hydroxide (NaOH), and anhydrous ethanol (C_2H_6O) were of analytical grade and purchased from Sinophelic Chemical Reagents Co., Ltd. (Shanghai, China) Potassium hydroxide (KOH), acetylene black, polyvinylidene fluoride (PVDF), and N-methylpyrrolidone (C_5H_9NO) were also of analytical grade and supplied by Shanghai Aladdin Biochemical Technology Co., Ltd. Nickel foam (1 mm thickness, 99.9% purity, ≥95% porosity) was used as the substrate and current collector for working electrode preparation. A glassy carbon electrode (model R502) served as the reference electrode, while a platinum foil electrode (model Pt 210) was used as the counter electrode.

2.2 Preparation of Tannin-Modified Phenolic Carbon Aerogel

To synthesize the tannin-modified phenolic resin, 15 g of condensed tannin, 15 g of phenol, 20 g of urea, and 108.1 g of 37 wt.% formaldehyde solution were added to a flat-bottomed flask. Subsequently, 1 mL of 10 $mol \cdot L^{-1}$ NaOH was introduced to the mixture as a catalyst, and the solution was stirred and reacted at 85°C for 1 h to yield a tannin–phenol–urea-based phenolic resin.

After the reaction, the resin was cooled to room temperature and diluted using 50 wt.% ethanol aqueous solutions at different resin-to-solvent mass ratios (1:1.0, 1:1.5, 1:2.0, 1:2.5, and 1:3.0) to obtain five dilution groups. Each mixture was further adjusted to the desired pH by adding 200 μL of 10 mol·L^{-1} NaOH. The resulting mixtures were transferred into sealed glass tubes and placed in an oven at 100°C for gelation and aging. After 7 days, tannin–urea-modified phenolic hydrogels were obtained.

The hydrogel used for SCD was placed in anhydrous ethanol for solution replacement. New anhydrous ethanol was replaced every day, and this process was repeated for 4 days. The hydrogels used for APD and FD were placed in ethanol aqueous solution for solution displacement. New solutions were replaced every day, and this process was repeated for 4 days. After complete solvent exchange, the hydrogel was subjected to one of three different drying methods—freeze-drying (FD), supercritical drying (SCD), or ambient pressure drying (APD)—for 48 h to obtain the corresponding TPUF-based organic aerogel. FD was frozen at −99°C for 24 h, with a vacuum degree of about 10 Pa, and dried for 24 h. APD was dried at 25°C at 1 atm for 24 h. The refrigeration temperature of SCD is 5°C, the supercritical temperature is 35°C, and the supercritical time is 60 min.

The dried samples were placed in a quartz boat and carbonized in a tubular furnace under nitrogen atmosphere. The temperature was raised at a rate of 5°C min^{-1} to 800°C and maintained for 2 h under a constant nitrogen flow rate of 80 mL min^{-1}. The resulting materials were denoted as tannin-modified phenolic carbon cryogels. The overall preparation process is illustrated in Fig. 1. To ensure the reliability and reproducibility of the results, for each drying method (freeze-drying, supercritical drying, and ambient pressure drying), three independent batches of samples were prepared following the same synthesis conditions.

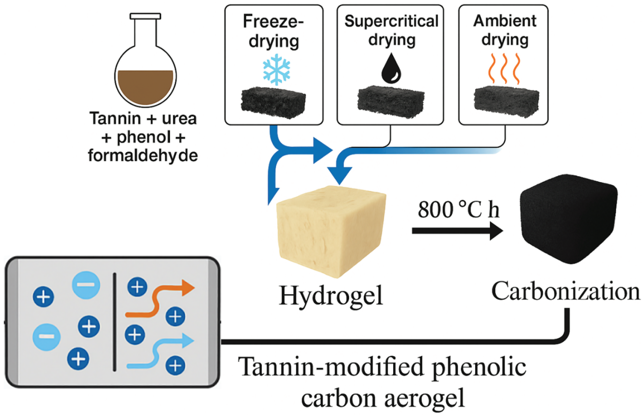

Figure 1: Schematic illustration of the preparation of tannin-modified phenolic carbon aerogels using three drying methods (FD, SCD, APD)

2.3 Characterization of TPUF Electrode Materials

The surface chemical composition and elemental valence states of the samples were analyzed by X-ray photoelectron spectroscopy (XPS, AXIS Ultra, Kratos Analytical, UK) using a monochromatic Al Kα radiation source (1486.6 eV) at a base pressure of 10^{-9} mbar. All binding energies were calibrated using the C 1s peak at 284.8 eV as the reference [25]. The crystalline structure and phase composition were determined via X-ray diffraction [26] (XRD, Bruker D8, Bragg–Brentano geometry). The specific surface area (SSA) and pore size distribution (PSD) were evaluated by nitrogen adsorption–desorption isotherms using an ASAP 2020 surface area and porosity analyzer (Micromeritics, USA). The Brunauer–Emmett–Teller

(BET) method was applied to determine SSA, while PSD was derived from the adsorption branch using the density functional theory (DFT) model. The morphology and microstructure of the carbon cryogels were examined using field-emission scanning electron microscopy (FE-SEM, Hitachi S3400) [27]. Fourier-transform infrared (FTIR) spectroscopy was carried out using a Bruker Tensor 27 spectrometer in the wavenumber range of 4000–400 cm^{-1}. The spectra were collected at a resolution of 4 cm^{-1} with 32 scans per sample using the KBr pellet method.

2.4 Electrochemical Measurement

The TPUF samples, acetylene black, and polyvinylidene fluoride (PVDF) were mixed in an agate mortar at a mass ratio of 8:1:1 and ground thoroughly to form a homogeneous powder. N-methylpyrrolidone (NMP) was added as a dispersant, and grinding was continued to obtain a uniform and viscous black slurry [28]. The resulting slurry was evenly coated onto nickel foam (1 × 2 cm), with an active material area of 1 × 1 cm. The coated electrodes were dried in an oven at 80°C for 8–12 h and then pressed using a roller press to form the working electrode.

Electrochemical tests were conducted using a Zennium Electrochemical Workstation (Zahner, Germany). A standard three-electrode (3E) configuration was adopted, with 6 M KOH aqueous solution as the electrolyte. The nickel foam with the active material served as the working electrode, a Hg/HgO electrode was used as the reference electrode, and a platinum foil was employed as the counter electrode [29]. The electrochemical performance of the electrodes was evaluated by cyclic voltammetry (CV), galvanostatic charge–discharge (GCD), and electrochemical impedance spectroscopy (EIS).

The specific capacitance (Cs, F g^{-1}) of the electrode was calculated from the GCD curves using the following equation:

$$Cs = (I \times t_d)/(m \times \Delta V) \tag{1}$$

where I (A) is the discharge current, t_d (s) is the discharge time, ΔV (V) is the operating voltage window, and m (g) is the mass of the active material on the electrode.

The SCS construction and electrochemical tests are performed as follows: The SCS electrode passes through the procedure described above for the working electrode. Two electrodes with similar mass of TPUF-FD were selected as positive and negative electrodes, respectively. SCS were constructed using a 6 M KOH solution as an electrolyte for electrochemical electro-chemical impedance testing. The mass ratio of the positive to negative electrode loadings was calculated using the following formulas:

$$q^{+} = q^{-} \tag{2}$$

$$q = mC\Delta v \tag{3}$$

$$m^{+}/m^{-} = C\Delta V^{-}/C\Delta V^{+} \tag{4}$$

where m (g) represents the sample mass loaded on the foam nickel electrode sheet, C (F g^{-1}) is the specific capacitance calculated based on the GCD curve of the supercapacitor, and V(V) is the voltage window. The formula for calculating ED (Wh kg^{-1}) and PD (W kg^{-1}) of supercapacitors is as follows:

$$ED = \left(C \times \Delta V^2\right)/7.2 \tag{5}$$

$$PD = (E \times 3600)/t_d \tag{6}$$

$$\eta = t_d/t_c \tag{7}$$

where η represents the Coulomb efficiency of the supercapacitor, t_d (s) is the discharge time, t_c (s) is the charging time, and V (V) is the voltage window of the device [30].

3 Results and Discussion

3.1 Morphological and Chemical Properties

Fig. 2 presents SEM images of the TPUF-based carbon cryogels prepared using three distinct drying techniques: supercritical drying (SCD), freeze-drying (FD), and ambient pressure drying (APD). As shown in Fig. 2a,b, the sample prepared via SCD (TPUF-SCD) exhibits aggregated spherical particles forming loose, porous clusters. These structures generate visible meso- and macroporous voids between particles, which contribute to improved ion diffusion pathways and mitigated structural shrinkage during drying. By contrast, the freeze-dried cryogel (TPUF-FD), Fig. 2c,d shows a more uniform and densely interconnected network, with a higher abundance of micropores. The absence of capillary forces during the sublimation of frozen solvent effectively prevents network collapse, thereby preserving the gel's fragile framework. As a result, the TPUF-FD sample achieves enhanced specific surface area (SSA) and better pore accessibility, both of which are favorable for electrochemical applications. In Fig. 2e,f, the morphology of the aerogel obtained via APD (TPUF-APD) reveals a compact and partially collapsed structure. Significant pore shrinkage is evident, accompanied by a noticeable loss of porosity. This densification is primarily attributed to capillary pressure and surface tension during the solvent evaporation process, which often destroys both micro- and mesoporous structures. Collectively, these observations confirm that the drying method critically determines the microstructure and pore architecture of tannin-modified phenolic carbon cryogels. Among the three methods, freeze-drying proves to be the most effective in preserving a hierarchical porous framework—an essential feature for promoting efficient ion transport and superior electrochemical performance in supercapacitor electrodes [31].

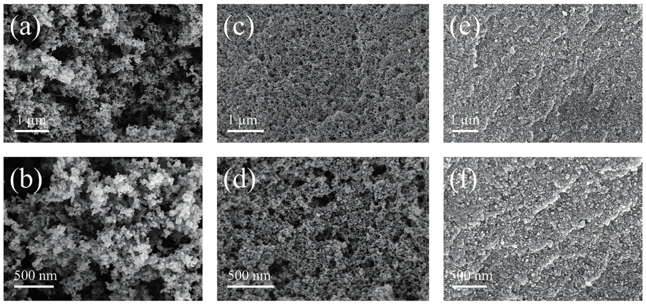

Figure 2: SEM images of carbon cryogels prepared via different drying methods: (**a**, **b**) TPUF-SCD (supercritical drying); (**c**, **d**) TPUF-FD (freeze-drying); (**e**, **f**) TPUF-APD (ambient pressure drying)

Fig. 3a presents the nitrogen adsorption–desorption isotherms of TPUF-based carbon cryogels obtained using different drying techniques. All samples exhibit hybrid characteristics of Type I and IV isotherms, indicating the coexistence of microporous and mesoporous structure [32,33]. At low relative pressures ($P/P_0 < 0.1$), the sharp increase in adsorption confirms the dominance of micropores, while the presence of H3-type hysteresis loops at higher relative pressures reflects slit-shaped mesopores commonly found in aggregated or layered materials [34]. Among the three drying strategies, the TPUF-FD sample exhibits the highest nitrogen uptake across the entire relative pressure range, revealing its superior porosity and largest specific surface area (788.42 m^2 g^{-1}), as summarized in Table 1. In this study, the enhanced performance of freeze-drying is attributed to its ability to preserve the delicate gel network without inducing thermal or pressure-driven shrinkage. During freeze-drying, the frozen solvent sublimates directly, avoiding capillary stresses that could collapse the pore structure. In contrast, the elevated temperature and pressure used in SCD may induce partial framework densification or collapse.

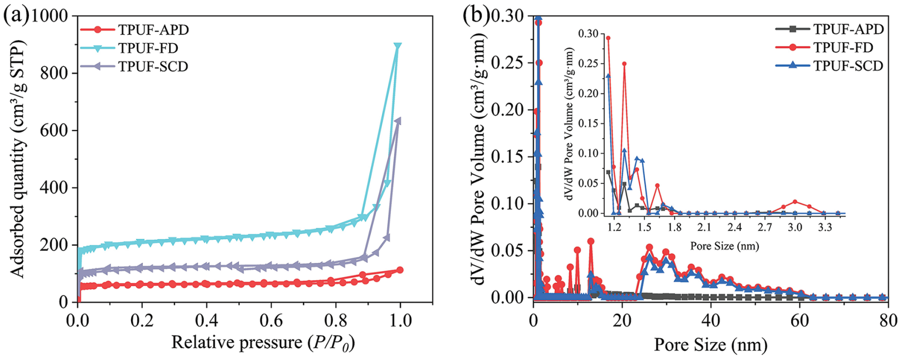

Figure 3: (**a**) Nitrogen adsorption–desorption isotherms of carbon cryogels prepared via different drying methods; (**b**) Corresponding pore size distribution curves (inset: magnified view of the micropore region, 1.0–3.5 nm)

Table 1: Pore structure parameters of TPUF carbon cryogels derived from N_2 adsorption–desorption analysis. Data are presented as the mean values of three independently prepared samples (n = 3)

Sample	S_{BET} (m^2/g)	$V_{0.99}$ (cm^3/g)	V_{DR} (cm^3/g)	L_0 (nm)	$V_{DR}/V_{0.99}$	V_{meso} (cm^3/g)
TPUF-SCD	436.57	0.98	0.17	0.79	0.17	0.81
TPUF-FD	788.42	1.39	0.31	0.70	0.22	1.08
TPUF-APD	235.45	0.17	0.09	0.63	0.51	0.08

This conclusion is further supported by the pore size distribution (PSD) profiles shown in Fig. 3b. The TPUF-FD exhibits a high volume of micropores in the 1.1–1.8 nm range, consistent with the steep low-pressure uptake observed in the isotherms. Additionally, it possesses the largest mesopore volume (1.08 cm^3 g^{-1}), which enhances ion diffusion kinetics during electrochemical operation. The presence of micropores provides high surface area and abundant adsorption sites for ion storage [35,36], while mesopores serve as ion diffusion channels. In contrast, macropores act as ion reservoirs facilitating electrolyte infiltration during charge–discharge processes. In contrast, ambient pressure drying (TPUF-APD) results in significant pore collapse, yielding the lowest specific surface area (235.45 m^2 g^{-1}) and severely limited microporosity due to capillary stress [37]. These findings confirm that freeze-drying, under appropriately designed dilution and gelation conditions, offers a more effective strategy than SCD for maintaining and enhancing the porous architecture of biomass-derived cryogels, thus maximizing their potential in high-performance energy storage applications.

Fig. 4a presents the X-ray diffraction (XRD) patterns of tannin-modified phenolic carbon cryogels prepared via three different drying methods. All three samples exhibit two broad diffraction peaks: the first centered at approximately 24.2°, corresponding to the (002) plane of turbostratic carbon, and the second around 44.1°, assigned to the (100)/(101) planes [38,39]. The broadness and low intensity of these peaks indicate that the materials are predominantly amorphous, lacking long-range graphitic order. Notably, the (002) peak position for all samples is slightly shifted toward lower angles compared to crystalline graphite (26.5°), which suggests a larger interlayer spacing. Based on Bragg's law, the calculated interlayer distance (d_{002}) is approximately 0.367 nm—significantly greater than the typical value for graphite (0.335 nm) [40]. This expansion reflects a disordered carbon structure with poorly stacked graphene layers, which is common for carbon materials derived from low-temperature carbonization of organic precursors. The similarity in XRD peak positions among all samples indicates that the drying method does not significantly affect the long-range crystal structure of the carbon cryogels.

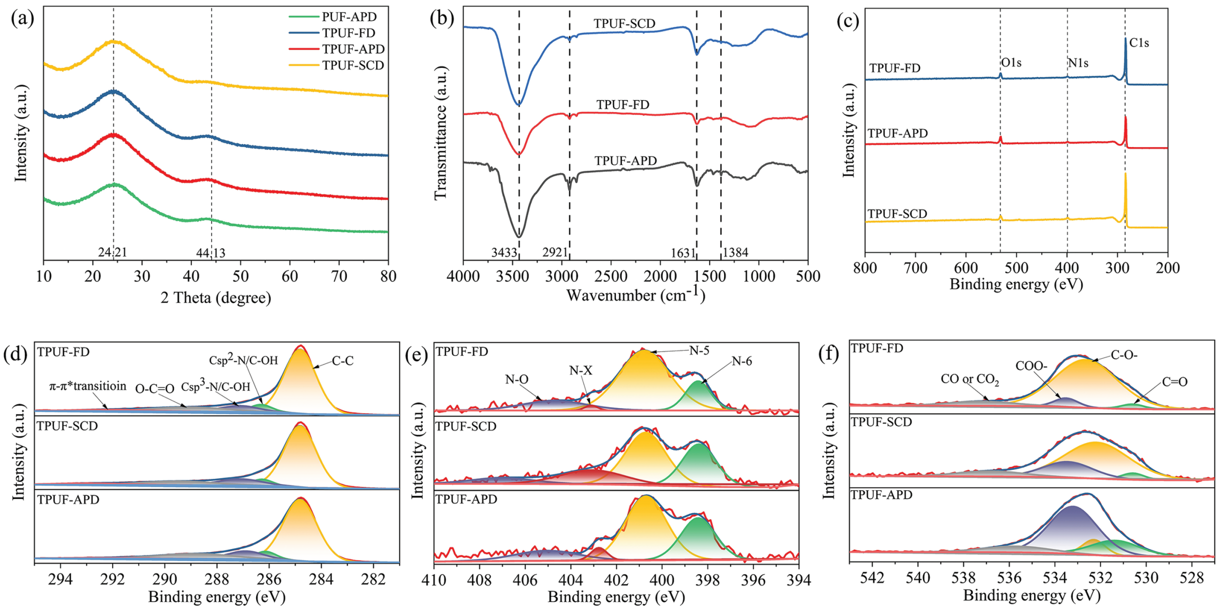

Figure 4: (**a**) XRD patterns; (**b**) FTIR spectra; (**c**) Survey XPS spectra; (**d**) High-resolution C 1s spectra; (**e**) High-resolution N 1s spectra; (**f**) High-resolution O 1s spectra of TPUF-based carbon cryogels prepared via different drying methods (FD, SCD, APD)

Fig. 4b shows the Fourier-transform infrared (FTIR) spectra of the TPUF-based carbon cryogels. All samples exhibit characteristic absorption bands corresponding to key functional groups retained after carbonization. The broad band at 3433 cm^{-1} corresponds to the stretching vibration of –OH groups, while the peak at 2921 cm^{-1} is attributed to the C–H stretching vibration of aliphatic hydrocarbons. The absorption at 1631 cm^{-1} arises from N–H bending vibrations, and the peak at 1384 cm^{-1} is assigned to C–N stretching, indicating the successful incorporation of nitrogen-containing functionalities into the carbon framework [41–43]. These functional groups are considered beneficial for enhancing the pseudocapacitive behavior and wettability of the carbon materials. The presence of similar spectral features across all drying methods suggests that the chemical structure of the aerogel backbone remains largely unaffected by the choice of drying technique.

Fig. 4c presents the X-ray photoelectron spectroscopy (XPS) survey spectra, confirming that carbon (C), nitrogen (N), and oxygen (O) are the major elements in all samples [44,45]. Their relative atomic percentages are summarized in Table 2. The carbon content ranges from 86.92 to 91.33 at%, while nitrogen and oxygen contents vary between 2.48–3.44 at% and 3.24–10.02 at%, respectively, depending on the drying technique employed. To further elucidate the surface functionalities and bonding environments, high-resolution XPS spectra were analyzed. As shown in Fig. 4e, the N 1s spectrum is deconvoluted into four distinct components: pyridinic-N (N-6, ~398.4 eV), pyrrolic-N (N-5, ~400.7 eV), quaternary-N (N-X, ~403.1 eV), and oxidized-N (N–O, ~404.7 eV) [46,47]. Among these, N-5 and N-6 are well-known for their electrochemical activity, promoting both pseudocapacitive reactions and enhanced electrical conductivity [48]. According to Table 2, TPUF-FD has the highest proportion of N-5 (68.70%) and N-6 (16.25%), which are favorable for improving supercapacitor performance. In contrast, SCD and APD samples show increased N-X and N–O fractions, indicating more structural disorder or oxidation during the drying process. Fig. 4d presents the deconvoluted C 1s spectra, revealing five main bonding states: C–C (284.8 eV), Csp^2–N/C–OH (286.3 eV), Csp^3–N/C=O (287.1 eV), O–C=O (289.1 eV), and the π–π^* shake-up transition (~290.1 eV) [49–51]. The FD sample shows a higher relative intensity of Csp^2–N/C–OH and Csp^3–N/C=O, indicating both an elevated degree of nitrogen doping and surface hydroxylation, which are beneficial for electrolyte wettability and surface redox reactivity. The O 1s spectra, as shown in Fig. 4f, are deconvoluted into four oxygen species: C=O (530.6 eV), C–O–C (532.6 eV), COO$^-$ (533.5 eV), and CO_2 or physisorbed CO (537.0 eV) [52,53]. Both TPUF-FD and TPUF-SCD show C–O–C as the dominant oxygen species, suggesting the formation of ether-like linkages that enhance thermal and electrochemical stability. In contrast, the APD sample contains a higher proportion of COO$^-$ groups, indicative of oxidative degradation and less structural stability. These results collectively show that freeze-drying leads to a more favorable surface chemistry, characterized by high electroactive N-5/N-6 content, low oxidized nitrogen, and stable C–O structures. These characteristics contribute synergistically to enhancing the conductivity, surface polarity, and electrochemical performance of the carbon cryogels.

Table 2: Relative elemental composition and nitrogen configurations in TPUF carbon cryogels synthesized by different drying methods

Sample	Relative element content/at%			The atomic ratio of different types of nitrogen/%			
	C	O	N	N-6	N-5	N-X	N-O
TPUF-FD	90.89	3.240	2.480	16.25	68.70	1.480	14.20
TPUF-APD	86.92	10.02	3.060	29.16	53.14	4.240	13.46
TPUF-SCD	91.33	5.230	3.440	29.15	44.13	18.89	7.830

3.2 *Electrochemical Performance*

The electrochemical properties of TPUF-FD, TPUF-SCD, and TPUF-APD were investigated using a three-electrode system in 6 M KOH electrolyte. Fig. 5a displays the CV curves of all samples at a scan rate of 20 mV s^{-1} within the potential window of –1.0 to 1.0 V. The curves exhibit a quasi-rectangular shape with distinguishable redox humps, indicating a combination of electric double-layer capacitance (EDLC) and pseudocapacitance. The pseudocapacitance arises from both oxygen-containing surface groups (e.g., –COOH and –OH) and nitrogen functionalities, particularly pyrrolic (N-5) and pyridinic (N-6) nitrogen atoms, which participate in reversible Faradaic redox reactions and enhance electrochemical activity [54–56]. Among the three, TPUF-FD exhibits the largest enclosed area under the CV curve, reflecting the highest charge storage capacity and prominent Faradaic contribution. Fig. 5b shows the CV curves of TPUF-FD at scan rates ranging from 5 to 200 mV s^{-1}. As the scan rate increases, the redox peaks shift slightly due to polarization effects, but the overall shape remains stable, indicating fast, reversible redox reactions and good rate capability [56]. The galvanostatic charge–discharge (GCD) curves at 0.5 A g^{-1} (Fig. 5c) further support the superior performance of TPUF-FD, which shows the longest discharge time and the most symmetric triangular profile, suggesting efficient and stable charge storage. Fig. 5d displays the GCD curves of TPUF-FD at various current densities. The specific capacitance (Cs) values were calculated to be 127.6, 122.3, 118.6, 113.0, and 107.0 F g^{-1} at 0.5, 1.0, 2.0, 5.0, and 10.0 A g^{-1}, respectively. The gradual decrease in Cs with increasing current density is attributed to ion diffusion limitations; at high current, electrolyte ions cannot fully penetrate into the inner pores of the electrode, thereby reducing capacitance [57].

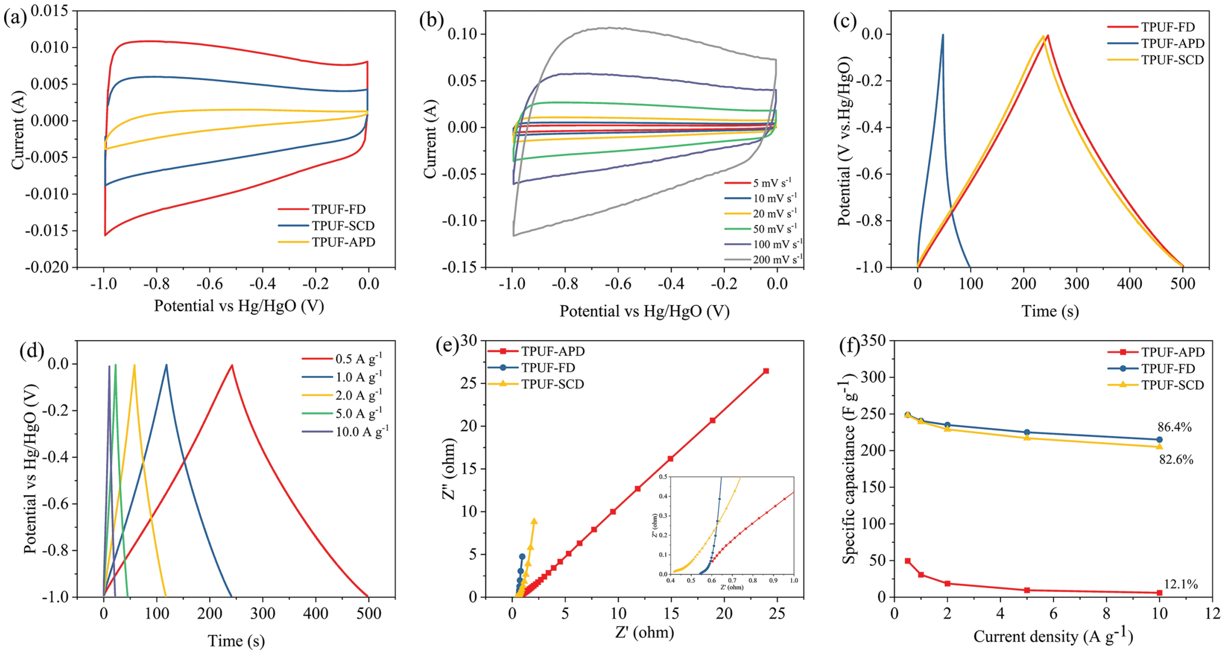

Figure 5: Electrochemical performance of TPUF-based carbon cryogels in a three-electrode system with 6 M KOH electrolyte: (**a**) CV curves of different samples at 20 mV s^{-1}; (**b**) CV curves of TPUF-FD at various scan rates (5–200 mV s^{-1}); (**c**) GCD curves of different samples at 0.5 A g^{-1}; (**d**) GCD curves of TPUF-FD at different current densities (0.5–10.0 A g^{-1}); (**e**) Nyquist plots from EIS measurements; (**f**) Specific capacitance retention at different current densities. Data represent average values from three independent measurements; error bars are omitted for clarity

Electrochemical impedance spectroscopy (EIS) results (Fig. 5e) reveal that TPUF-FD exhibits the smallest semicircle in the high-frequency region and the steepest slope in the low-frequency region, indicating lower charge transfer resistance and faster ion diffusion. This is due to its well-preserved hierarchical pore structure, including interconnected mesopores that provide efficient ion pathways.

Fig. 5f compares the capacitance retention of the three samples at increasing current densities. TPUF-FD maintains 83.9% of its capacitance at 10 A g^{-1}, followed by TPUF-SCD (79.8%) and TPUF-APD (only 11.8%). The remarkable rate capability of TPUF-FD demonstrates that freeze-drying is most effective in preserving the pore architecture, enhancing ion accessibility, and maintaining performance at high rates. These results demonstrate that among the three drying techniques, freeze-drying provides the optimal porous structure and surface chemistry required for high-performance supercapacitor electrodes. It is noteworthy that the difference in specific capacitance between TPUF-FD and TPUF-SCD is not as pronounced as expected based on their pore structure differences. These results suggest that electrochemical performance is governed not only by the extent of porosity but also by the accessibility and conductivity of the active surface. Thus, the interplay between pore architecture and microstructural ordering must be carefully considered when optimizing drying strategies for carbon aerogel-based supercapacitor electrodes.

3.3 *Symmetric Supercapacitor Device Performance*

To evaluate the practical application potential of the TPUF-FD carbon aerogel, a symmetric supercapacitor device (TPUF-FD//TPUF-FD) was assembled using two electrodes with matched mass loadings and 6 M KOH as the electrolyte [58]. Fig. 6a displays the CV curves of the device at various voltage windows ranging from 1.0 V to 1.5 V at a scan rate of 10 mV s^{-1}. The device maintains a nearly rectangular CV shape without significant distortion up to 1.5 V, indicating high electrochemical stability and suggesting that TPUF-FD is a promising material for high-voltage aqueous supercapacitors. As shown in Fig. 6b, the CV curves recorded at scan rates ranging from 10 to 200 mV s^{-1} exhibit broad quasi-rectangular shapes with noticeable redox peaks. This combination of electric double-layer behavior and Faradaic pseudocapacitance is consistent with the presence of oxygen- and nitrogen-containing surface functional groups, as demonstrated in XPS analysis. GCD curves obtained at different voltage windows (Fig. 6c) and current densities (Fig. 6d) show symmetric charge–discharge profiles, indicating excellent reversibility and coulombic efficiency. At 0.5 A g^{-1} under a 1.5 V voltage window, the device achieves a specific capacitance of 27.1 F g^{-1}. With increasing current density, the specific capacitance gradually decreases to 11.0 F g^{-1} at 10 A g^{-1}, as expected due to ion transport limitations at higher charge/discharge rates. Importantly, no voltage drops or polarization is observed, suggesting efficient electron and ion transport and strong interfacial compatibility between electrode and electrolyte [59].

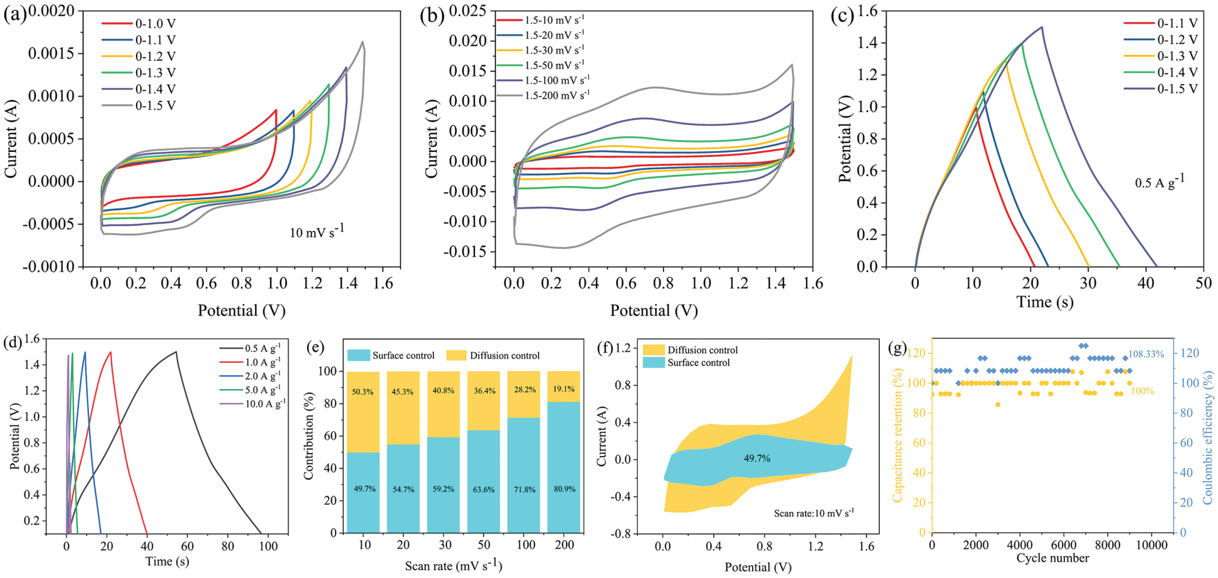

Figure 6: Electrochemical performance of the symmetric supercapacitor assembled with TPUF-FD electrodes in 6 M KOH electrolyte: (**a**) CV curves at different voltage windows (0–1.0 to 0–1.5 V) at 10 mV s^{-1}; (**b**) CV curves at various scan rates (10–200 mV s^{-1}); (**c**) GCD curves at different voltage windows at 0.5 A g^{-1}; (**d**) GCD curves at different current densities (0.5–10 A g^{-1}); (**e**) Capacitance contribution from surface-controlled and diffusion-controlled processes at various scan rates; (**f**) Surface-controlled contribution map at 10 mV s^{-1}; (**g**) Cycling performance and coulombic efficiency at 10 A g^{-1}

To further investigate the charge storage mechanism, the relative contributions of surface-controlled and diffusion-controlled processes were quantified using CV data. As shown in Fig. 6e, the surface-controlled contribution increases with scan rate [60], reaching over 79.8% at 200 mV s^{-1}, confirming rapid ion kinetics and accessibility of active sites. Fig. 6f shows that at 10 mV s^{-1}, 49.7% of the current response originates from surface-controlled processes, highlighting the dual storage mechanism.

The energy and power density of the symmetric device were calculated to be 8.47 Wh kg^{-1} and 562.5 W kg^{-1} at 0.5 A g^{-1} and 1.5 V, respectively. Comparing the electro-chemical performance of our ASC with other literature reports, the results are presented in Table 3, demonstrating the superior Energy density and Power density of the constructed SCs in our study. Finally, the cycling stability of the TPUF-FD symmetric device was assessed at 10 A g^{-1} over 9000 charge–discharge cycles (Fig. 6g). Impressively, the device maintained 100% of its initial capacitance, and its coulombic efficiency remained above 100%, reflecting excellent structural integrity, stable electrode–electrolyte interfaces, and highly reversible charge storage. These results outperform many similar systems reported in the literatures, confirming the practical applicability of TPUF-FD for long-life, high-performance supercapacitor devices.

Table 3: Comparison of electrochemical properties of different SCs

SCs	Energy density (Wh kg^{-1})	Power density (W kg^{-1})	Current density (A g^{-1})	Specific capacitance (F g^{-1})	Refs.
TPUF-FD//TPUF-FD	8.47	562.5	0.5	127.6	This work
DLPFC//DLPFC	3.9	125.0	0.5	112.4	[55]
CC//CC	3.4	24.0	0.1	99.0	[61]
SNAC-1//SNAC-1	5.42	500	0.5	162.0	[62]

4 Conclusion

In this study, a bio-derived tannin-modified phenolic carbon aerogel (TPUF-FD) was successfully fabricated through partial substitution of phenol with sustainable tannin and processed using three different drying strategies to evaluate their impact on final microstructure and electrochemical performance. Among them, the freeze-drying (FD) method proved most effective in preserving the gel's porous architecture, preventing collapse of the fragile network structure, and facilitating the formation of a hierarchical micro–mesoporous system. This resulted in superior specific surface area and ion transport dynamics. The TPUF-FD electrode demonstrated a high specific capacitance of 127.6 F g^{-1} at 0.5 A g^{-1} and retained 83.9% at 10 A g^{-1} in a three-electrode configuration, significantly outperforming the samples prepared via ambient or supercritical drying. When assembled into a symmetric device, the supercapacitor exhibited an energy density of 8.47 Wh kg^{-1} at a power density of 562.5 W kg^{-1}, and delivered exceptional long-term cycling stability, maintaining 100% capacitance retention and 108.33% coulombic efficiency after 9000 cycles. This work demonstrates not only the structural benefits of freeze-drying for carbon cryogel fabrication but also the cost-effectiveness and sustainability of tannin as a biomass precursor. Moreover, it provides a comparative framework for evaluating the influence of drying strategies on porous carbon materials. Moving forward, further enhancement of TPUF-based electrodes could be achieved through heteroatom doping (e.g., N, S, P), incorporation of conductive nanostructures (e.g., graphene, MXene), and optimization of hydrogel polymerization conditions. In addition, future research should consider scaling up the preparation process and conducting techno-economic analysis to assess the feasibility of commercial applications in energy storage devices such as flexible or hybrid supercapacitors.

Acknowledgement: The authors also thank Shyamji Lab (www.shiyanjia.com) for the assistance in the XPS tests.

Funding Statement: We gratefully acknowledge the support of the central government guides local funds for scientific and technological development (2023L3044), the Natural Science Foundation of Fujian Province, China (Grants

2023J01462), Fujian Agriculture and Forestry University Science and Technology Innovation Special Fund Project (Grants KFB23142, KFB24010).

Author Contributions: Zhiying Lin: Conceptualization, data curation, methodology, writing—original draft. Boju Deng: Data curation, investigation, methodology, software. Qianqian Zhang: Conceptualization, investigation, methodology. Jingming Chen, Xinqiang Ye: Conceptualization, investigation. Mizi Fan: Methodology, resources. Yuling Lan: Conceptualization, methodology, project administration, writing—review & editing. Jiuping Rao, Weigang Zhao: Conceptualization, project administration, resources, supervision, writing—original draft, writing—review & editing. All authors reviewed the results and approved the final version of the manuscript.

Availability of Data and Materials: The data that support the findings of this study are available from the corresponding authors upon reasonable request.

Ethics Approval: Not applicable.

Conflicts of Interest: The authors declare no conflicts of interest to report regarding the present study.

References

1. Wang Z, Tammela P, Strømme M, Nyholm L. Cellulose-based supercapacitors: material and performance considerations. Adv Energy Mater. 2017;7(18):1700130. doi:10.1002/aenm.201700130.
2. Shrestha A, Ali Mustafa A, Htike MM, You V, Kakinaka M. Evolution of energy mix in emerging countries: modern renewable energy, traditional renewable energy, and non-renewable energy. Renew Energy. 2022;199:419–32. doi:10.1016/j.renene.2022.09.018.
3. Zhang Q, Lin Z, Deng B, Luo L, Rao J, Du G, et al. Chloride-ion-engineered nickel-cobalt bimetallic chloride: a tunable electrode material for high-energy-density supercapacitors. J Power Sources. 2025;633:236378. doi:10.1016/j.jpowsour.2025.236378.
4. Zhang Q, Wang S, Lan Y, Deng J, Fan M, Du G, et al. Enhancing supercapacitor electrochemical performance through acetate-ion intercalation in layered nickel–cobalt double hydroxides. J Colloid Interface Sci. 2024;660(4):597–607. doi:10.1016/j.jcis.2024.01.105.
5. Wang S, Deng J, Li M, Lin J, Luo L, Yuan Z, et al. Nitrogen-Doped tannin carbon dots anchored NiCo-LDH composites for high-performance asymmetric supercapacitors. Chem Eng J. 2025;511(1):162275. doi:10.1016/j.cej.2025.162275.
6. Poonam, Sharma K, Arora A, Tripathi SK. Review of supercapacitors: materials and devices. J Energy Storage. 2019;21:801–25. doi:10.1016/j.est.2019.01.010.
7. Wang S, Lin J, Yuan Z, Luo L, Zhang W, He C, et al. Tunable architecture of cobalt-nickel metal-organic framework/activated carbon composites for superior electrochemical performance in asymmetric supercapacitors. J Colloid Interface Sci. 2025;684:647–57. doi:10.1016/j.jcis.2025.01.002.
8. Lan Y, Wang S, Yuan Z, Zhao W. NiCo layered double hydroxide anchored on MXene/tannin carbon cryogel composite with 3D hierarchical sea urchin-like structure for asymmetric supercapacitors. Chem Eng J. 2024;501(14):157471. doi:10.1016/j.cej.2024.157471.
9. Sruthy ES, Grimm A, Paul M, Cherian CT, Thyrel M, Molaiyan P, et al. Low-temperature highly graphitized porous biomass-based carbon as an efficient and stable electrode for lithium-ion batteries and supercapacitors. Chem Eng J Adv. 2025;22:100762. doi:10.1016/j.ceja.2025.100762.
10. Jagdale SD, Rao CRK, Bhosale SV, Bhosale SV. An azo functionalized anthraquinone as organic electrode materials for efficient pseudocapacitors with excellent cycling stability. J Energy Storage. 2024;80:110323. doi:10.1016/j.est.2023.110323.
11. Ma Y, Yuan W, Bai Y, Wu H, Cheng L. The toughening design of pseudocapacitive materials via graphene quantum dots: towards enhanced cycling stability for supercapacitors. Carbon. 2019;154(32):292–300. doi:10.1016/j.carbon.2019.07.095.

12. Zhou Y, Luo L, Yan W, Li Z, Fan M, Du G, et al. Controlled preparation of nitrogen-doped hierarchical carbon cryogels derived from Phenolic-Based resin and their CO_2 adsorption properties. Energy. 2022;246(1):123367. doi:10.1016/j.energy.2022.123367.
13. Li ZL, Zhou YL, Yan W, Luo L, Su ZZ, Fan MZ, et al. Cost-effective monolithic hierarchical carbon cryogels with nitrogen doping and high-performance mechanical properties for CO_2 capture. ACS Appl Mater Interfaces. 2020;12(19):21748–60. doi:10.1021/acsami.0c04015.
14. Guo X, Gong R, Qin N, Jin L, Zheng J, Wu Q, et al. The influence of electrode matching on capacity decaying of hybrid lithium ion capacitor. J Electroanal Chem. 2019;845:84–91. doi:10.1016/j.jelechem.2019.05.046.
15. Cheng H, Xue H, Hong C, Zhang X. Preparation, mechanical, thermal and ablative properties of lightweight needled carbon fibre felt/phenolic resin aerogel composite with a bird's nest structure. Compos Sci Technol. 2017;140:63–72. doi:10.1016/j.compscitech.2016.12.031.
16. Matović B, Gorshkova YE, Kottsov SY, Kopitsa GP, Butulija S, Minović Arsić T, et al. Carbon cryogel preparation and characterization. Diam Relat Mater. 2022;121(12):108727. doi:10.1016/j.diamond.2021.108727.
17. Wang T, Liu Z, Li P, Wei H, Wei K, Chen X. Lignin-derived carbon aerogels with high surface area for supercapacitor applications. Chem Eng J. 2023;466:143118. doi:10.1016/j.cej.2023.143118.
18. Xiao Z, Yu J, Feng M, Meng L, Yang C, Guo W. Three-dimensional biochar aerogel anode derived from expired yogurt for enhancing power efficiency and electron transfer at the bacteria-anode interface in microbial fuel cells. J Environ Chem Eng. 2024;12(3):113009. doi:10.1016/j.jece.2024.113009.
19. Luo L, Lan Y, Zhang Q, Deng J, Luo L, Zeng Q, et al. A review on biomass-derived activated carbon as electrode materials for energy storage supercapacitors. J Energy Storage. 2022;55:105839. doi:10.1016/j.est.2022.105839.
20. Lyu J, Park J, Kumar Pandey L, Choi S, Lee H, De Saeger J, et al. Testing the toxicity of metals, phenol, effluents, and receiving waters by root elongation in *Lactuca sativa* L. Ecotoxicol Environ Saf. 2018;149(2):225–32. doi:10.1016/j.ecoenv.2017.11.006.
21. Zhao W, Deng J, Li M, Du G, Fan M, Gao H, et al. Rational synthesis of sea urchin-like NiCo-LDH/tannin carbon microsphere composites using microwave hydrothermal technique for high-performance asymmetric supercapacitor. Adv Compos Hybrid Mater. 2025;8(2):215. doi:10.1007/s42114-025-01220-5.
22. Braghiroli FL, Fierro V, Szczurek A, Stein N, Parmentier J, Celzard A. Hydrothermally treated aminated tannin as precursor of N-doped carbon gels for supercapacitors. Carbon. 2015;90(3):63–74. doi:10.1016/j.carbon.2015.03.038.
23. Miyamoto R, Ueoka R, Tachibana K, Maeno A, Kaji H, Kanamori K. Monolithic poly(methylsilsesquioxane) aerogels with glasslike transparency: from Sol-gel synthesis to ambient pressure drying. J Sol Gel Sci Technol. 2024;112(1):202–15. doi:10.1007/s10971-024-06528-0.
24. Guo Y, Su J, Bian T, Yan J, Que L, Jiang H, et al. Construction and application of carbon aerogels in microwave absorption. Phys Chem Chem Phys. 2023;25(12):8244–62. doi:10.1039/d2cp05715h.
25. Isaacs MA, Davies-Jones J, Davies PR, Guan S, Lee R, Morgan DJ, et al. Advanced XPS characterization: xps-based multi-technique analyses for comprehensive understanding of functional materials. Mater Chem Front. 2021;5(22):7931–63. doi:10.1039/d1qm00969a.
26. Wang J, Xiang L, Ren C, Huang T, Zhu Y, Wei P, et al. Quantitative determination of quaternary solid waste-based binders and its hydrates by XRD. Constr Build Mater. 2024;425(4):135888. doi:10.1016/j.conbuildmat.2024.135888.
27. Hiscock M, Lang C, Statham P, Bauer F, Hartfield C. Enhancing materials and device analysis capability in the SEM and FIB-SEM by using a nanomanipulator. Microsc Microanal. 2016;22(S3):16–7. doi:10.1017/s1431927616000933.
28. Liu C, Lei T, Seidi F, Ahmad M, Cao D, Yu Z, et al. Multiscale wood-derived materials for advanced supercapacitors: from macro to micro and nano. Energy Storage Mater. 2024;72(18):103774. doi:10.1016/j.ensm.2024.103774.
29. Zhang P, Chen Y, Song X, Zhang H, Cui J, Wang B. Preparation of hierarchical porous carbon from corncob hydrochar by KCl enhancing K_2CO_3 activation for electrode material of supercapacitor. Chem Eng J. 2025;503:157703. doi:10.1016/j.cej.2024.157703.
30. Khan R, Ryu C, In JB. Fabrication of modified laser-induced graphene using activated carbon and polyamic acid coating for flexible and high-performance microsupercapacitors. Carbon. 2024;230(100):119646. doi:10.1016/j.carbon.2024.119646.

31. Chu G, Zhao J, Huang Y, Zhou D, Liu Y, Wu M, et al. Phosphoric acid pretreatment enhances the specific surface areas of biochars by generation of micropores. Environ Pollut. 2018;240:1–9. doi:10.1016/j.envpol.2018.04.003.
32. Li Y, Wei Z, Zhan Z, Pei J, Zhao C, Xu W, et al. Scale-up biomass strategy to macro-microporous nitrogen-doped carbon aerogels for ionic liquid supercapacitors with high efficiency. J Energy Storage. 2024;76:109778. doi:10.1016/j.est.2023.109778.
33. Buttersack C. General cluster sorption isotherm. Microporous Mesoporous Mater. 2021;316:110909. doi:10.1016/j.micromeso.2021.110909.
34. Zhu X, Hope-Weeks LJ, Baghi R, Charles VR, Yu Y, Zhu L, et al. Enhanced compressive strength of carbon aerogels with low density and high specific surface areas. J Porous Mater. 2022;29(4):1279–85. doi:10.1007/s10934-022-01254-w.
35. Shree Kesavan K, Surya K, Michael MS. High powered hybrid supercapacitor with microporous activated carbon. Solid State Ion. 2018;321:15–22. doi:10.1016/j.ssi.2018.04.005.
36. Sayed MS, Aman D, Fayed MG, Omran MM, Zaki T, Mohamed SG. Unravelling the role of pore structure of biomass-derived porous carbon in charge storage mechanisms for supercapacitors. RSC Adv. 2024;14(34):24631–42. doi:10.1039/d4ra04681a.
37. Brandão AT, State S, Costa R, Potorac P, Vázquez JA, Valcarcel J, et al. Renewable carbon materials as electrodes for high-performance supercapacitors: from marine biowaste to high specific surface area porous biocarbons. ACS Omega. 2023;8(21):18782–98. doi:10.1021/acsomega.3c00816.
38. Zhang Z, Wang Z, Lu J, Lyu J, Zhuge X, Luo K, et al. Enhancing electrochemical performance of aluminum-oxygen batteries with graphene aerogel cathode. Small Meth. 2024;8(7):2301225. doi:10.1002/smtd.202301225.
39. Platek-Mielczarek A, Beda A, Fic K, Matei Ghimbeu C. Synthesis and performance of binder-free porous carbon electrodes in electrochemical capacitors. J Mater Chem A Mater. 2024;12(11):6412–25. doi:10.1039/d3ta04971j.
40. Reshma RP, Abishek NS, Gopalakrishna KN. Synthesis and characterization of graphene oxide, tin oxide, and reduced graphene oxide-tin oxide nanocomposites. Inorg Chem Commun. 2024;165(1):112451. doi:10.1016/j.inoche.2024.112451.
41. Ye D, Lv H, Zheng Z, Luo L. Preparation and properties of flexible phenolic silicone hybrid aerogels for thermal insulation. Molecules. 2024;29(20):4942. doi:10.3390/molecules29204942.
42. Liu Y, Deng Z, Zhang W, Jiang G, Cao W, Huang Z, et al. Lightweight, high-strength, heat-resistant TiB2–B4C-modified phenolic aerogel/carbon fiber composites with excellent thermal stability, oxidation, and ablation resistance for thermal protection. Adv Compos Hybrid Mater. 2024;8(1):24. doi:10.1007/s42114-024-01106-y.
43. Shan G, Cui M, Wang X, Gao Y, Xu Z, Jiang L, et al. Dual-reinforcement strategy: fabrication of CMC-Na/SPI aerogel-templated oleogels through electrostatic adsorption and chemical crosslinking. Food Hydrocoll. 2024;148(10):109525. doi:10.1016/j.foodhyd.2023.109525.
44. Nahar A, Akbor MA, Rahman MA, Ferdous Z, Hasan MR, Kamruzzaman S, et al. Enhanced electrochemical performance of waste newspaper derived activated carbon aerogel electrode for the supercapacitor. Results Eng. 2025;25:104043. doi:10.1016/j.rineng.2025.104043.
45. Dai L, Yang M, Jiang S, Tang H, Ren E, Xiao H, et al. N-doped lignin-based activated carbon aerogel derived from bamboo black pulp liquor for efficient removal of malachite green in wastewater. Env Sci Pollut Res. 2024;31(39):51325–43. doi:10.1007/s11356-024-34564-4.
46. Zhai Z, Li H, Zheng Y, Ji Y, Peng H, Gao Y, et al. High specific surface area carbon aerogel derived from starch for methylene blue adsorption and supercapacitors. Int J Biol Macromol. 2024;274(5):133282. doi:10.1016/j.ijbiomac.2024.133282.
47. Zhang Y, Wang L, Jia D, Yue L, Zhang H, Liu J. Hierarchical porous doped carbon plates derived from chitosan aerogel as cathode for high performance Zn-ion hybrid capacitor. ChemElectroChem. 2023;10(4):e202200972. doi:10.1002/celc.202200972.
48. Li H, Ma Y, Wang Y, Li C, Bai Q, Shen Y, et al. Nitrogen enriched high specific surface area biomass porous carbon: a promising electrode material for supercapacitors. Renew Energy. 2024;224(5):120144. doi:10.1016/j.renene.2024.120144.

49. Mian MM, Kamana IML, An X, Abbas SC, Ahommed MS, He Z, et al. Cellulose nanofibers as effective binders for activated biochar-derived high-performance supercapacitors. Carbohydr Polym. 2023;301(17):120353. doi:10.1016/j.carbpol.2022.120353.
50. Ge Y, Xu G, Wang Y, Zhong J, Fang Z, Zhang S, et al. A rigid free-standing supercapacitor electrode material made from fat coal-based activated carbon foam. Chem Eng J. 2024;491(24):151553. doi:10.1016/j.cej.2024.151553.
51. Zhang W, Bao Y, Bao A. Preparation of nitrogen-doped hierarchical porous carbon materials by a template-free method and application to CO_2 capture. J Environ Chem Eng. 2020;8(3):103732. doi:10.1016/j.jece.2020.103732.
52. Zhou Q, Qin L, Liu H, Zhao D, Yang M, Sun B, et al. Microwave assisted biomass derived carbon aerogel for highly efficient oxytetracycline hydrochloride degradation: singlet oxygen mechanism and C vacancies accelerated electron transfer. Chem Eng J. 2024;487:150370. doi:10.1016/j.cej.2024.150370.
53. Li K, Zhou M, Liang L, Jiang L, Wang W. Ultrahigh-surface-area activated carbon aerogels derived from glucose for high-performance organic pollutants adsorption. J Colloid Interface Sci. 2019;546:333–43. doi:10.1016/j.jcis.2019.03.076.
54. Nazhipkyzy M, Kurmanbayeva G, Seitkazinova A, Varol EA, Li W, Dinistanova B, et al. Activated carbon derived from cucumber peel for use as a supercapacitor electrode material. Nanomaterials. 2024;14(8):686. doi:10.3390/nano14080686.
55. Li P, Yang C, Yi D, Li S, Wang M, Wang H, et al. Preparation of spherical porous carbon from lignin-derived phenolic resin and its application in supercapacitor electrodes. Int J Biol Macromol. 2023;252(11):126271. doi:10.1016/j.ijbiomac.2023.126271.
56. Zhang Y, Chen Y, Liang K, Zhang Y, Wang D, Wang W, et al. NiCo layered double hydroxide/biomass-derived porous carbon aerogel composite for high-performance hybrid supercapacitors. J Energy Storage. 2024;91:112167. doi:10.1016/j.est.2024.112167.
57. Shan X, Guo Z, Qu Z, Zou Y, Zhao L, Chen P. Boosting the performance of nickel-cobalt LDH cathode with phosphorus and selenium co-doping for hybrid supercapacitor. Mater Res Lett. 2022;10(9):593–601. doi:10.1080/21663831.2022.2077149.
58. Wang P, Zhang G, Li MY, Yin YX, Li JY, Li G, et al. Porous carbon for high-energy density symmetrical supercapacitor and lithium-ion hybrid electrochemical capacitors. Chem Eng J. 2019;375:122020. doi:10.1016/j.cej.2019.122020.
59. Li M, Ding Y, Zhang S, Sun Y, Liu M, Zhao J, et al. Interface polarization effects enhancing Mn_2O_3@TiO_2@MXene heterostructures for aqueous magnesium ion capacitors: guided charge distribution and transportation via built-in electric fields. Small Struct. 2024;5(2):2300371. doi:10.1002/sstr.202300371.
60. Ali SR, Iqbal MZ, Faisal MM, Alzaid M. Diffusion control and surface control mechanism in hierarchical nanostructured porous zinc-based MOF material for supercapattery. Int J Energy Res. 2022;46(10):14424–35. doi:10.1002/er.8169.
61. Zhang Y, Cai Y, Li T, Wang M, Chen X, Xu Y. Synthesis and electrochemical performance of biomass-derived porous carbon materials for supercapacitors. J Mater Sci Mater Electron. 2024;35(2):116. doi:10.1007/s10854-024-11944-7.
62. Abbas SC, Lin C, Hua Z, Deng Q, Huang H, Ni Y, et al. Bamboo-derived carbon material inherently doped with SiC and nitrogen for flexible supercapacitors. Chem Eng J. 2022;433(9):133738. doi:10.1016/j.cej.2021.133738.